Chapter 6

Results

The results of this work can be divided into two broad categories: measurements of the meridional circulation; and measurements of the rotation and other zonal flows. This chapter is therefore divided into two corresponding sections. I begin with the section on the rotation, since it allows for some explanation of the methods and a comparison with more established techniques in helioseismology. The most important new results in this work can be found in section 6.2 on the observations of the meridional circulation.

6.1 Rotation and Zonal Flows[1]

For the purposes of measuring the rotation deep in the solar convection zone, I used measurements from 792 days of Structure images. The maximum distance used in the cross correlations was 19.2°, which corresponds to a turning radius of $0.88\,R_\odot$.

6.1.1 Inversion method and regularization

The discussion in chapter 5 shows that the solution of equation 2.44 for the internal velocity $u(r, \lambda)$ involves the choice of a particular regularization scheme and then a

[1]Early versions of these results appeared in the conference proceedings of IAU Symposium 185 (Giles and Duvall, 1998) and the SOHO6/GONG98 Workshop (Giles et al., 1998). Additional results have been presented in oral or poster form at the GONG99 Workshop and other conferences.

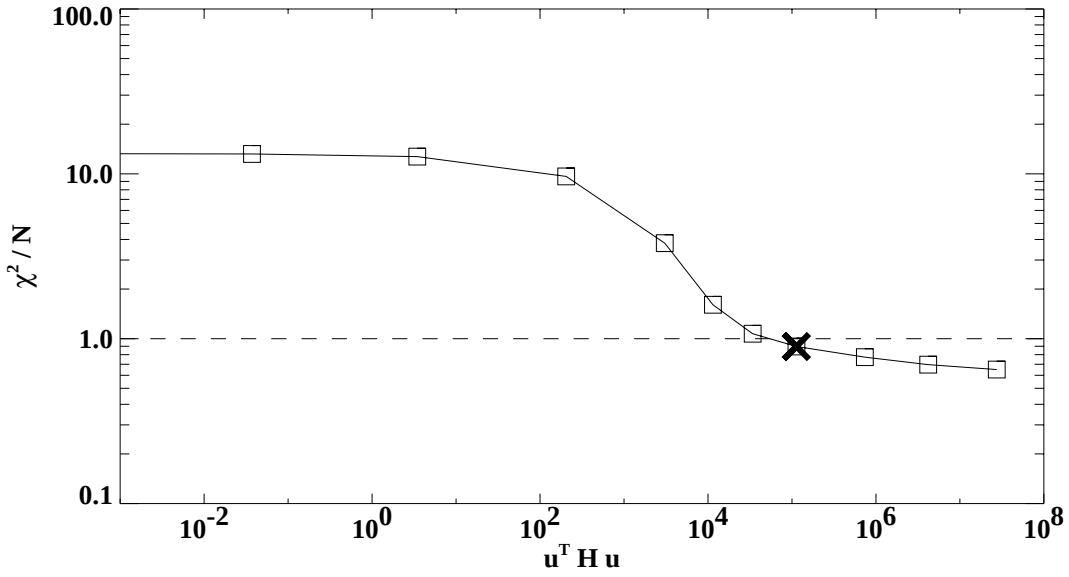

Figure 6.1: This L-curve shows the relationship between the "smoothness" and the "goodness-of-fit" of the solutions to an inversion for the rotation velocity. The dashed line marks the point where χ^2 (see equation 5.7) is equal to the number of measurements. The horizontal axis represents the deviation from perfect smoothness, with $u^T H u$ being mathematically described by equation 5.13. The point marked with $\times$ marks the solution which is shown in figures 6.2 and 6.3.

choice of trade-off parameter which gives the "best" solution. This necessarily involves some *a priori* assumptions about the real velocity profile in the Sun.

For the results presented here, the matrix H in equation 5.14 was chosen to be H_Ω from equation 5.13. The tradeoff parameter γ was then chosen by examining a trade-off curve like the one shown in figure 6.1. In this plot, each square represents a solution of equation 5.14 for a particular choice of γ, which is increasing from right to left. The solutions on the right side of the plot fit the data best, but are not physically appealing because of the large gradients in velocity. The solutions on the left side are very smooth but do not fit the measurements.

There are several criteria which can be used for choosing the best value of γ using the L-curve in figure 6.1. First, the optimal compromise between "smoothness" and "goodness-of-fit" can be achieved by choosing a solution near the bend in the L.

Once we have achieved such a solution, any further increase in the magnitude of the regularization causes a relatively small improvement in smoothness, at the expense of a large decrease in the agreement with the measurements. Furthermore, if the measurement errors have been reliably determined, then the chosen solution should have a value of χ^2 which is roughly equal to the number of measurements; this then gives the solution which is as smooth as possible and yet still fits the data by some objective criterion.

In this particular case, the inversion results can be compared to the known internal rotation, as determined from normal mode frequency splittings. This is the method that has been used to choose a particular solution from the set of solutions depicted in figure 6.1. The symmetric part of the time-distance solution has been compared with a solution from the MDI frequency splittings (Larsen, 1999). It is reassuring that this solution is also near the bend in the L, and that the calculated χ^2/N is close to 1. The consistency of these different criteria lend confidence to the estimated measurement errors and to the final results. The value of χ^2/N is 0.90, which I interpret as an indication that the estimated measurement errors are slightly too large.

6.1.2 Comparison to modal approach

Since the use of the time-distance method to measure flows is a relatively new area of scientific exploration, it is useful to compare the results of this method with the results of the more well-established modal approach. As outlined in section 2.2.1, the global approach in helioseismology yields information about the component of the angular velocity which is symmetric about the solar equator. Therefore, for the purpose of comparison it is necessary to take the symmetric part of the time-distance results.

The inversion techniques outlined in chapter 5 give a reconstruction of the velocity as a function of radius and latitude; this can be converted to an angular frequency by the formula

$$\frac{\Omega}{2\pi}\,[\mathrm{nHz}] = v\,[\mathrm{m/s}]\,\frac{10^9}{r\cos\lambda}. \tag{6.1}$$

I then obtain the symmetric part of $\Omega/2\pi$ by calculating the mean of the velocities

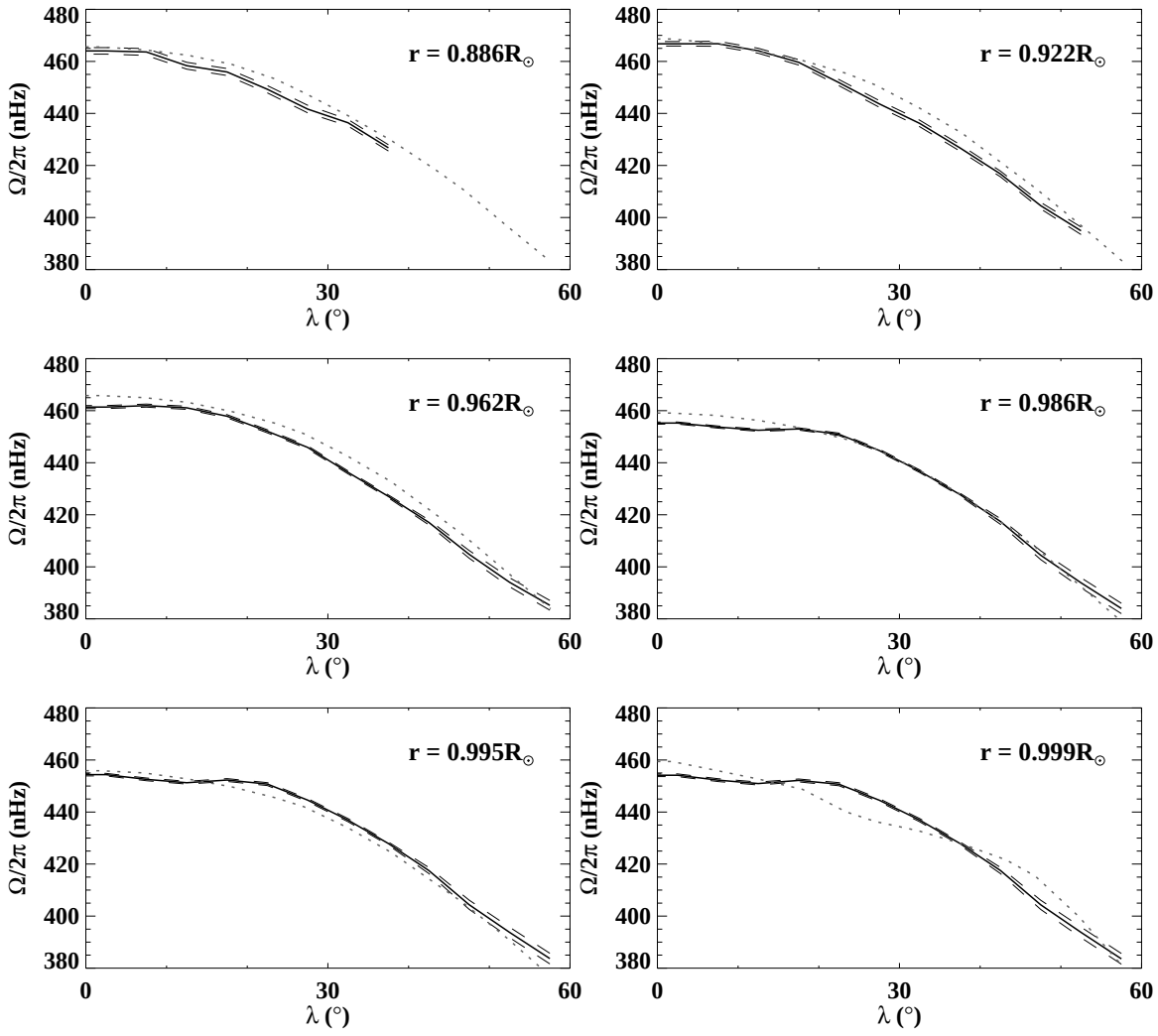

Figure 6.2: Comparison of the time-distance and normal mode methods for determining the solar rotation. The angular frequency is plotted versus latitude for six different choices of radial coordinate. The dotted curve is the result of an OLA inversion of MDI frequency splittings. The solid curve is the symmetric component of the time-distance result from this work; the dashed lines are the formal errors from the inversion.

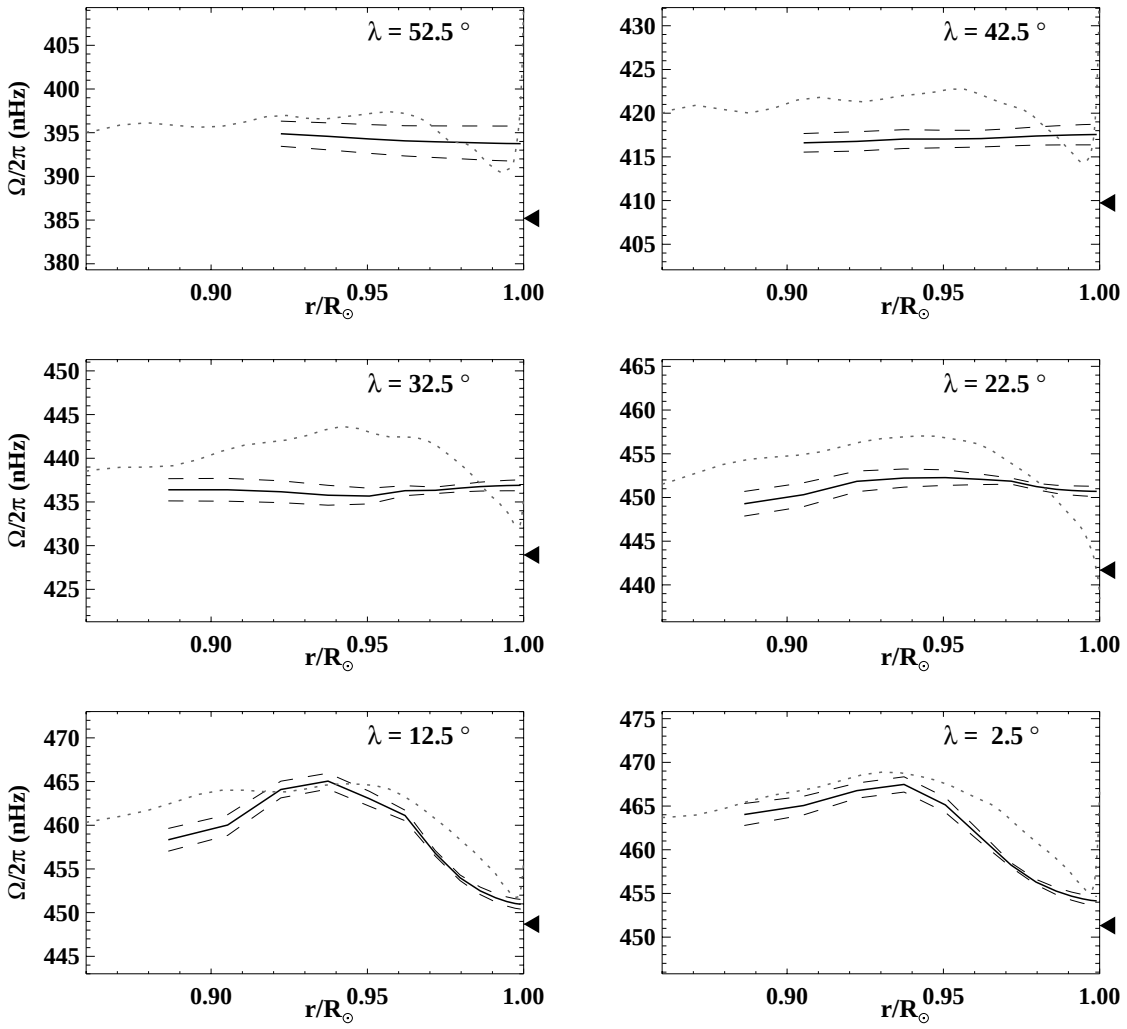

Figure 6.3: Comparison of the time-distance and normal mode methods for determining the solar rotation. The angular frequency is plotted versus radius for six different latitudes. The dotted curve is the result of an OLA inversion of MDI frequency splittings. The solid curve is the time-distance result from this work; the dashed lines are the formal errors from the inversion. The arrow on the right-hand axis in each plot represents the surface rotation rate from Snodgrass (1984).

in the northern and southern hemispheres, weighted by the formal errors from the inversion. For comparison, I use an OLA inversion of the MDI frequency splittings[2] The frequency splittings were measured from 144 days of Structure program images, and the inversion results extend to below the bottom of the convection zone; only the region which overlaps with the time-distance results is presented here.

Figures 6.2 and 6.3 show a quantitative comparison of the two measured profiles. The first set of figures shows the angular velocity as a function of latitude, for different depths; obviously, the time-distance method can accurately capture the differential rotation. The plots for the smallest values of r do not extend as far in latitude because of geometrical considerations which limit the maximum travel distance. In both figures 6.2 and 6.3, the dashed lines represent the formal errors (one standard deviation) from the time-distance inversion, calculated as described in section 5.2.5. The errors for the frequency splitting result are on the order of 1 nHz, which is so small as to be unimportant in the comparison.

Although figure 6.2 shows that there is good qualitative agreement between the two methods, the large range of angular velocities means that the differences between the two measurements can be hidden. These differences can be more clearly seen in figure 6.3, where the angular velocity is plotted, as a function of radius, for different latitudes. At low latitude, the two results are in good qualitative agreement; at higher latitudes, the agreement is not as good.

In figures 6.2 and 6.3, it should be noted that the "flattening" of the angular velocity seen, for example, at high latitudes, is characteristic of the particular choice of the regularization matrix $H = H_\Omega$ in equation 5.14. The regularization, if allowed to act independently of any measurements, will give an angular velocity which is uniform everywhere. This is the "default" solution in regions where the model is essentially unconstrained by the data, either due to large measurement errors or low sensitivity.

Another way to think about this behaviour is in terms of spatial averaging kernels,

[2]The OLA inversion result and averaging kernels were provided by R. M. Larsen. Although different inversion techniques and different instruments give slightly different results for the frequency measurements (Schou et al., 1998), at the level of precision considered here all the inversions are identical.

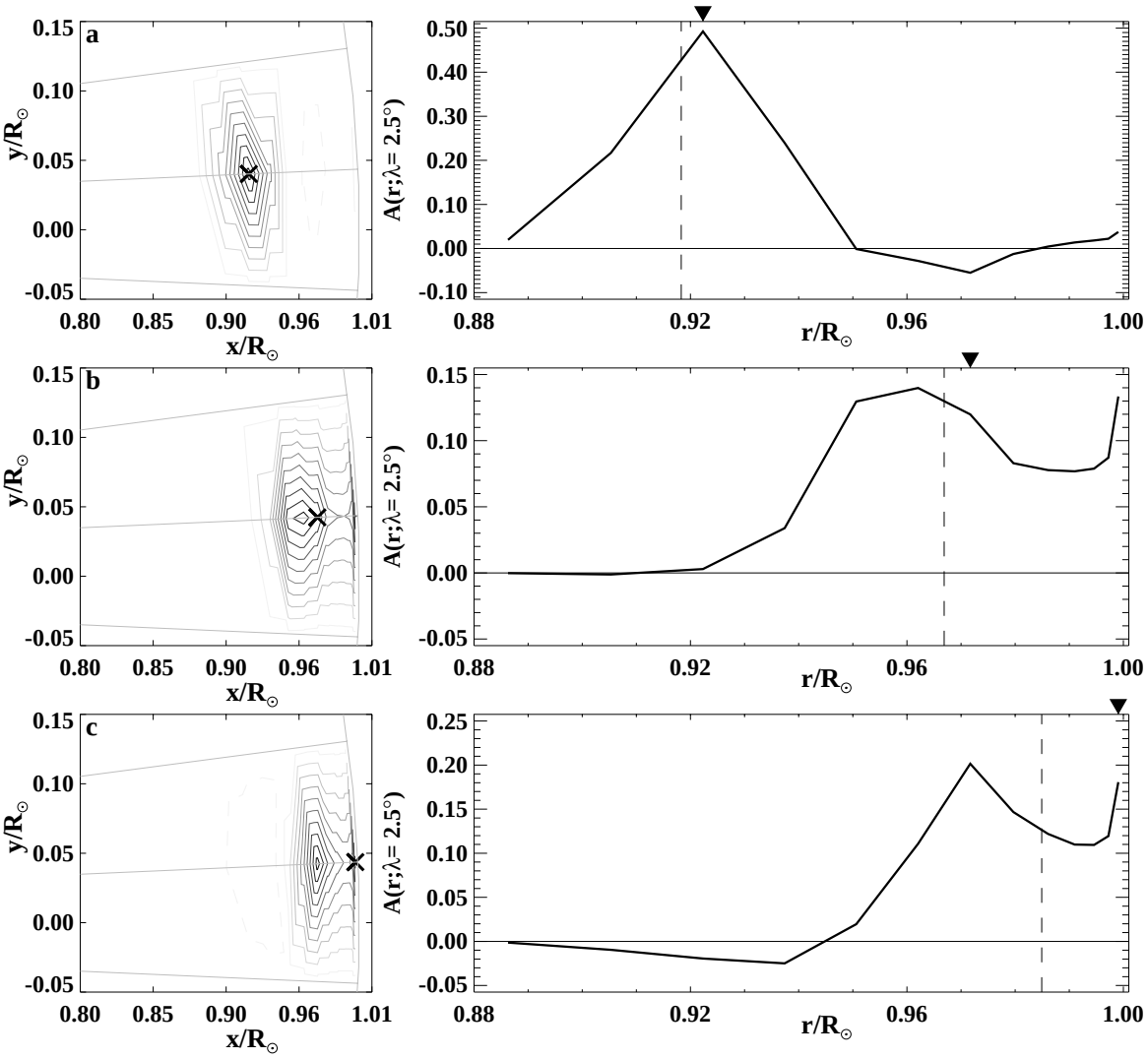

Figure 6.4: Selected averaging kernels for the time-distance inversion in figures 6.2 and 6.3. The plots in the left-hand column are contour plots of three different averaging kernels. The contour spacing is 5% of the maximum amplitude of each kernel; dashed contour lines indicate a negative amplitude. The nominal locations for the three kernels, marked with the symbol $\times$, are: (a) $r = 0.920\,\mathrm{R}_\odot, \lambda = 2.5°$; (b) $r = 0.966\,\mathrm{R}_\odot, \lambda = 2.5°$; and (c) $r = 0.986\,\mathrm{R}_\odot, \lambda = 2.5°$. In the right-hand column, a cross section of each kernel is plotted, as a function of radius, at the central latitude. The arrow on each plot marks the nominal radius of the kernel; the dashed line marks the location of the centroid.

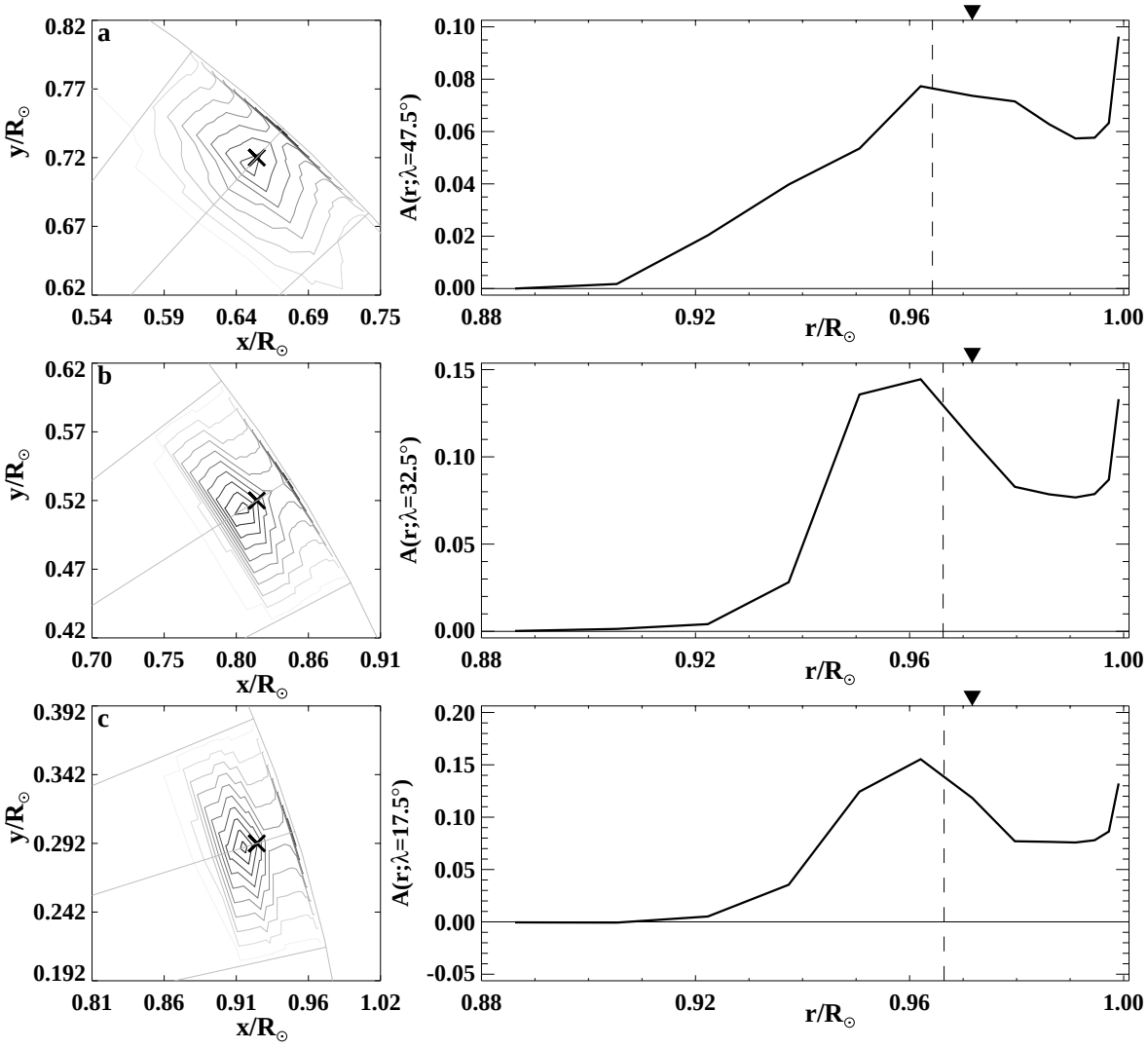

Figure 6.5: Selected averaging kernels for the time-distance inversion in figures 6.2 and 6.3. The symbols and contours are the same as for figure 6.4. In this case the kernels all have the same nominal radius $r = 0.966\,\mathrm{R}_\odot$, but different latitudes: (a) $\lambda = 47.5°$; (b) $\lambda = 32.5°$; and (c) $\lambda = 17.5°$. Note for comparison that the nominal radius is also the same as for figure 6.4(b).

as outlined in section 5.2.4. To make a more even comparison between the two methods, it is important to examine the differences between the averaging kernels. Figures 6.4 and 6.5 show selected averaging kernels for the time-distance inversion. One striking feature of the averaging kernels is that they are very well localized in latitude. If we recall that each averaging kernel is created from a weighted sum of the sensitivity kernels, this is perhaps not surprising (a typical sensitivity kernel is shown in figure 5.1). However, it should be noted as an advantage of this method over the frequency-splitting approach. In fact, the latitude resolution in this case is limited by the extent of the averaging used in making the measurements; because I averaged together all the cross correlations for five-degree bands of latitude, the averaging kernels cannot be narrower than five degrees in that dimension.

In the radial direction, on the other hand, the averaging kernels are not well localized; in fact, in some regions they have very small amplitudes near their nominal location. Again, this is related to the shape of the sensitivity kernels. For example, the shortest travel distance included in this analysis is $\Delta = 3°$; the lower turning point for a ray with this travel distance is about $0.98\,R_\odot$. Since the ray sensitivity kernels are rather small between the upper and lower turning points, it is not possible to construct an averaging kernel which is localized between about $0.98\,R_\odot$ and the surface.

Given the width of the averaging kernels, it is perhaps not surprising that there are some significant differences between the two different profiles in figures 6.3. One way to compare the two methods more evenly is to convolve the frequency splitting result with the averaging kernels from the time-distance result, and vice versa. This results in two models with comparable (although very poor) resolution.

Figure 6.6 shows the results of this comparison. Clearly there is great improvement in the agreement between the two models. Direct comparison of the averaging kernels shows that although the time-distance kernels span a narrower range in latitude, the modal kernels in general have smaller sidelobes and better resolution in the radial direction. Since the OLA (Optimally Localized Averaging) technique is explicitly designed to construct well-behaved averaging kernels, this is perhaps not surprising. A similar approach might be applied to the time-distance measurements

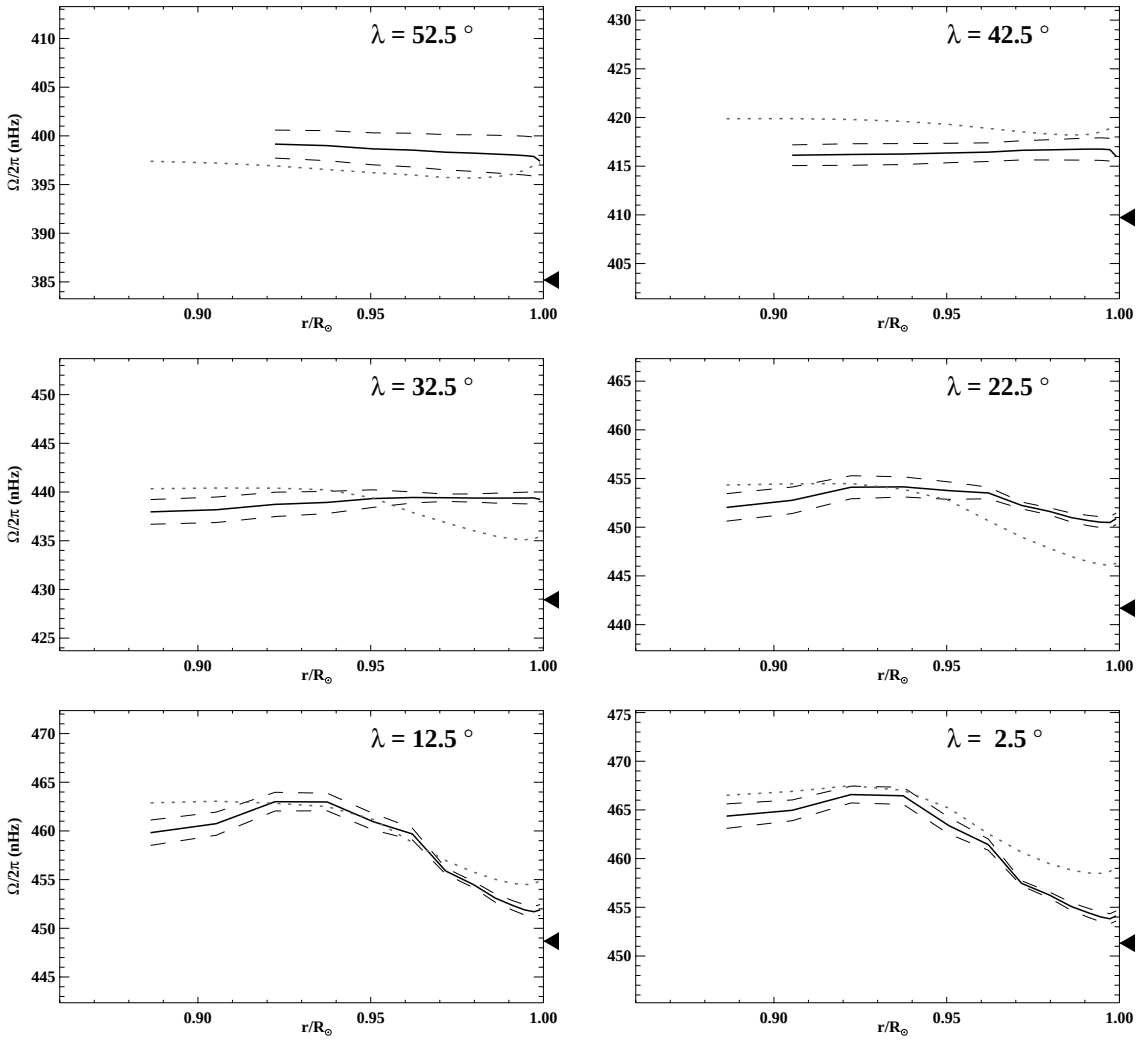

Figure 6.6: The comparison in figure 6.3 is repeated here, but the frequency splitting result (dotted line) has been convolved with the averaging kernels from the time-distance inversion, and vice versa, reducing the spatial resolution of both models so that the two methods are comparable in that regard.

in the future. The construction and optimization of inversion techniques in analysis of mode frequency splittings has been an area of vigorous study in helioseismology for nearly fifteen years; it is hoped that the expertise gathered in this research can be applied to the time-distance method as well.

6.1.3 North-south asymmetry

The comparison with the modal approach, while a useful check on the method, is not very interesting from a scientific point of view. After all, the modal approach to determining rotation — having nearly a decade head start — is unlikely to be surpassed in the first attempt. However, it is possible to learn something new about the solar rotation by looking for asymmetries between the northern and southern hemispheres.

A first step is to examine the measurements themselves. Figures 6.7 and 6.8 show the complete set of time differences for the rotation study. These measurements were made over the 792-day Structure run by the process outlined in chapter 4. The sense of the time difference is (east − west), so that a positive time difference reflects a flow in the prograde (westward) direction.

To look for asymmetries between the two hemispheres, the measurements have been divided into two groups. The open circles represent the measurements for the northern hemisphere, and the filled circles for the southern hemisphere. The measurements for particular latitudes fall along distinct curves because the velocity decreases rapidly as the latitude increases. Thus, the points with the largest time differences are for measurements made near the equator, and the smaller time differences are for measurements closer to the poles. It should be stated that this spreading is largely removed by the image tracking procedure mentioned in section 4.1. The removed velocities have here been added back into the data using the known interior profile (from global helioseismology) and the ray sensitivity kernels calculated for the time-distance inversion[3].

As might be expected, the measurements from the two hemispheres in figure 6.7

[3]Since the model interior profile is symmetric, the time differences added on are also symmetric.

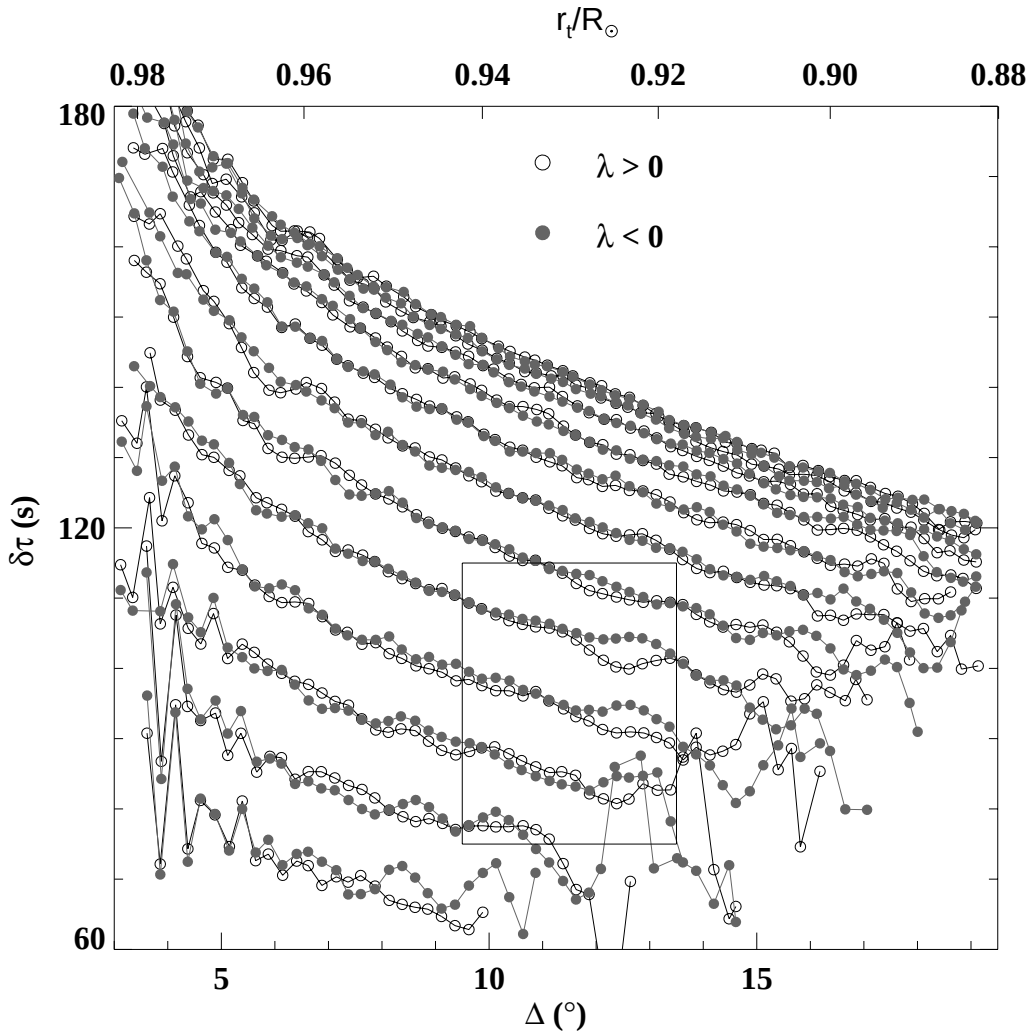

Figure 6.7: Measurements of the time differences from 792 days of MDI Structure program Dopplergrams. The vertical axis shows the time difference, in seconds, between eastward- and westward-propagating waves; the horizontal axis on the bottom shows the travel distance, in degrees. The upper horizontal axis shows the turning point r_t for rays which travel a distance Δ between surface reflections. The open circles are for measurements in the northern hemisphere, and the filled circles for measurements in the southern hemisphere. The interesting feature inside the small box is shown in more detail in figure 6.8.

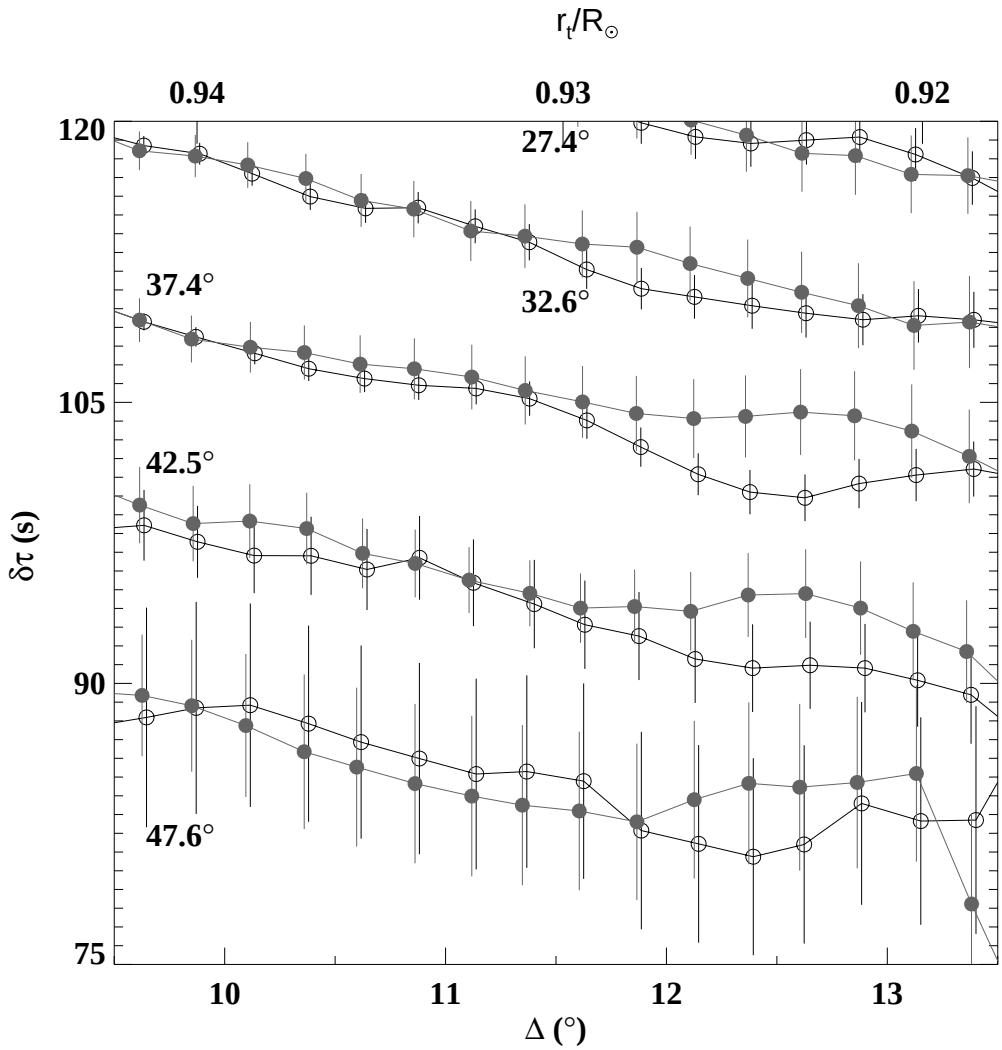

Figure 6.8: A smaller region of figure 6.7 has been replotted here, with measurement errors. Again the open circles are for measurements in the northern hemisphere, and filled circles for the southern hemisphere. Measurements for particular latitudes have been joined together by line segments; the latitude for each set of measurements is indicated on the left-hand side of the figure. The measurements fall along well-separated curves, reflecting the decrease in the zonal velocity at higher latitudes. There is an interesting and significant asymmetry noted between the northern and southern hemispheres, localized above 35° latitude and near a radius of $0.925\,R_\odot$.

generally agree quite well with each other. However, one obvious deviation from this symmetry can be seen in some of the measurements near $\Delta = 12.5°$. This region has been expanded in figure 6.8. There is a marginally significant difference between the northern and southern hemispheres for latitudes between 30 and 50 degrees and distances between 12 and 13 degrees. These distances correspond to rays with turning points near $r = 0.925\,\mathrm{R}_\odot$. The amplitude of the difference is about 4 seconds, or roughly 3% of the surface rotation rate at that latitude. Since the time difference is accumulated as the integral along the ray path, the local perturbation must be considerably larger than this.

It is worth noting that the measurement process is exactly symmetric about the equator, with two exceptions. The first is that the solar B_0 angle[4] varies during the course of the year, which causes the oscillation signal at high latitudes to vary in strength, due to line-of-sight projection effects. The measurements shown here were made over a period slightly longer than two years, so the effect of this asymmetry should be small. Second, the image scale[5] is not accurately known and may not be exactly symmetric. However, any north-south differences in the plate scale should be quite small. At any rate, it is difficult to imagine a distortion which would give rise to such a localized asymmetry in the measurements.

The evidence therefore points to an asymmetry in the rotation of the solar interior. To estimate the location and magnitude of this perturbation, I have created a series of velocity profiles with different asymmetric perturbations. The "reference" model was the result of the frequency splitting inversions presented in figures 6.2 and 6.3. To this profile I then added a localized perturbation which was positive (fast) in the northern hemisphere and negative (slow) in the southern hemisphere. The perturbation is described by the smooth function

$$v_p = A \exp\left[-\frac{(r - r_p)^2}{2\,\delta r^2}\right] \exp\left[-\frac{(\lambda - \lambda_p)^2}{2\,\delta\lambda^2}\right]. \tag{6.2}$$

With this perturbation added to or subtracted from the reference velocity, I then

[4]See also the discussion in appendix A.

[5]See also the discussion in section 4.7.2.

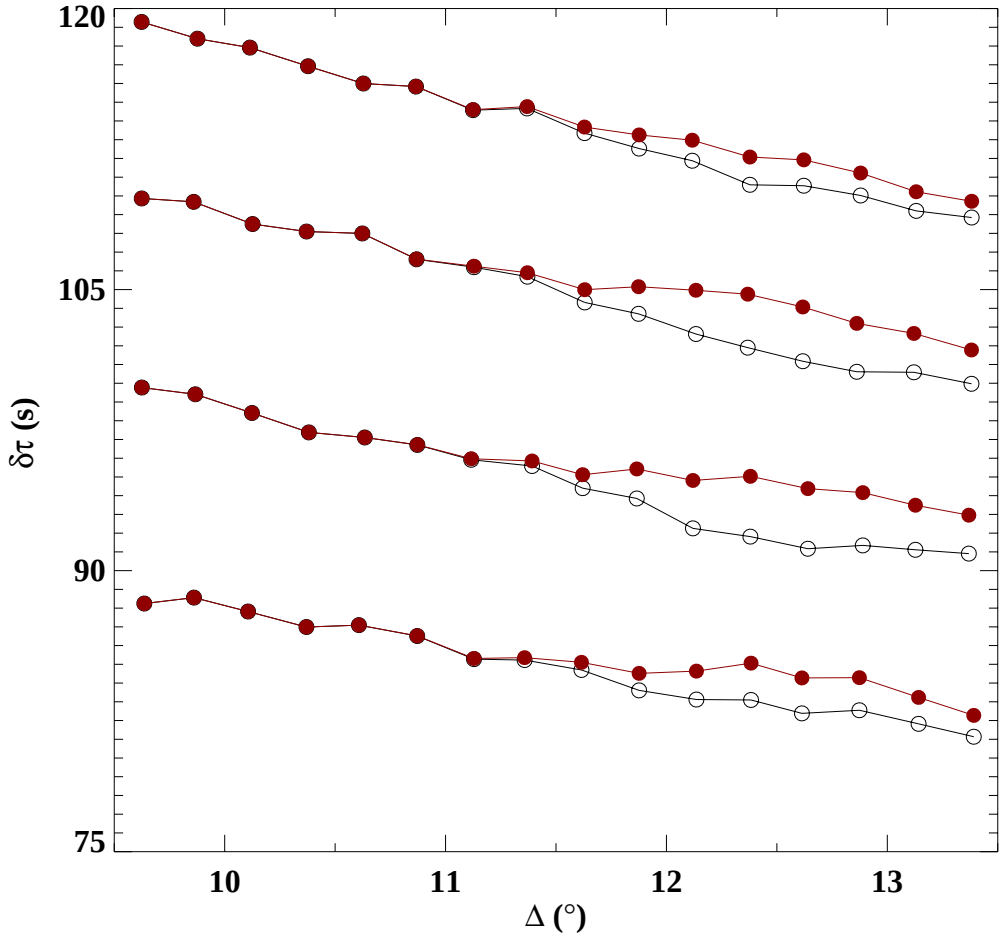

Figure 6.9: Travel time differences $\delta\tau$ have been calculated as a function of distance Δ for an asymmetric rotation profile. The velocity profile used was the frequency-splitting measurement of the internal rotation, with a localized perturbation added in each hemisphere as described in the text. The set of measurements chosen is the same as that in figure 6.8.

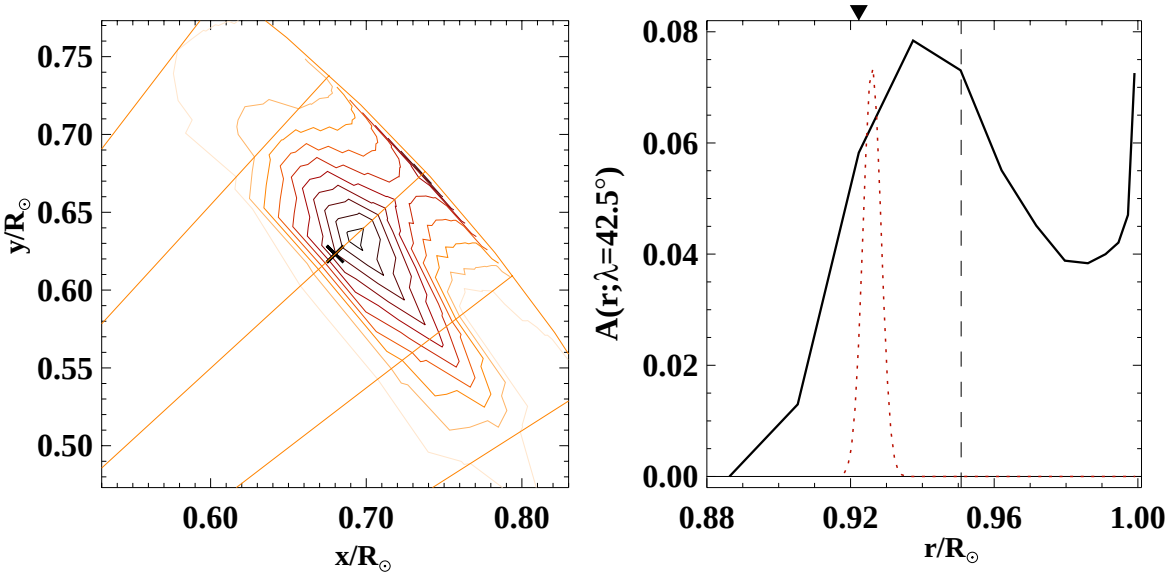

Figure 6.10: The left-hand figure shows the averaging kernel for $r = 0.920\,\mathrm{R}_\odot$ and $\lambda = 42.5°$, which is where the postulated asymmetry in the rotation is localized. The contour levels are 5% of the kernel amplitude, as in figures 6.5 and 6.4. The right-hand plot shows the radial cross section. The dotted curve shows the shape of the cross section of the perturbation which was used to create figure 6.9.

calculated the travel time differences for the set of measurements shown in figure 6.8. The results for one such perturbation v_p are shown in figure 6.9. For this particular case, I used the parameters $A = 200\,\mathrm{m/s}$, $r_p = 0.926\,\mathrm{R}_\odot$, $\delta r = 0.0025\,\mathrm{R}_\odot$, $\lambda_p = 41.0°$, and $\delta\lambda = 6.0°$. The general behaviour seen in figure 6.8 is reproduced quite well by this model, in particular the fact that the time differences are quite well-localized in latitude and distance, and that there appears to be no significant asymmetry for distances shorter than about 11.5°. The magnitude of the perturbation is quite large — about 14% of the unperturbed velocity at (r_p, λ_p). Also, the perturbation is extremely narrow in the radial direction, with a full width at half maximum of only 4×10^6 m.

Unfortunately, such a perturbation is impossible to find in the inversions described in section 6.1.2. The problem is essentially one of spatial resolution; figure 6.10 shows

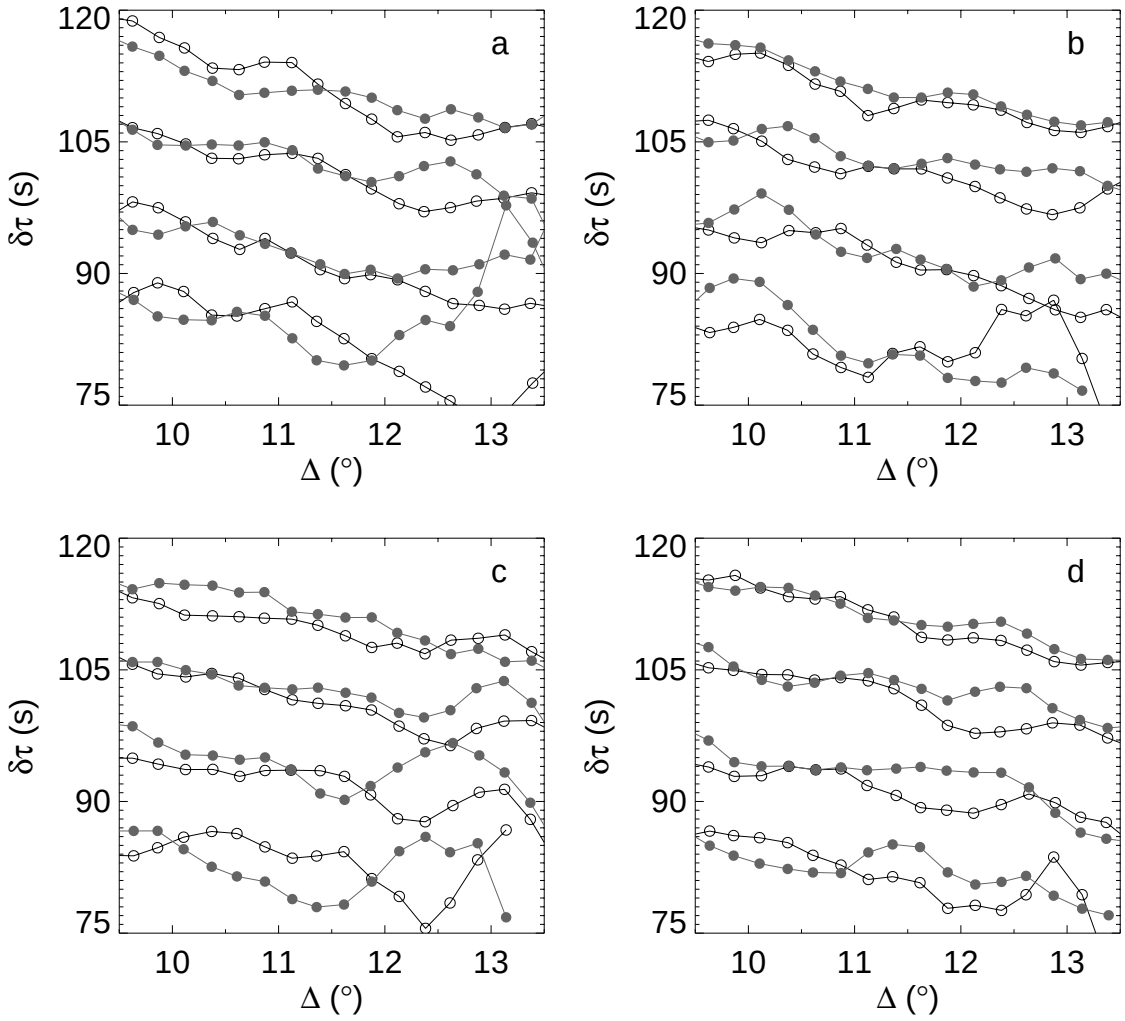

Figure 6.11: The measurements from figure 6.8 have been made for four six-month intervals: (a) May to November, 1996; (b) November, 1996 to May, 1997; (c) May to November, 1997; (d) November, 1997 to June, 1998. The latitude of each curve is the same as for figure 6.8, and again the open circles are for the northern hemisphere and the filled circles for the southern. For the two central curves (latitudes 37.4° and 42.5°), the rotation is persistently higher in the southern hemisphere than in the northern.

the averaging kernel for $\lambda = 42.5°, r = 0.920\,R_\odot$. Clearly the narrow asymmetric perturbation shown in the right-hand panel is not going to be resolved.

In light of the fact that solar activity changed quite dramatically over the two years of observation, it is interesting to ask whether the asymmetry in the rotation rate was present during the whole period. Figure 6.11 shows the same set of measurements as figure 6.8, but this time the time series has been divided into four time intervals. The four plots show that although the location and magnitude of the asymmetry vary somewhat, the sense and rough magnitude are basically constant over the time period in question.

6.1.4 Torsional oscillation

Since the torsional oscillation is a time-varying phenomenon, it is necessary to make time-resolved observations of the rotation velocity in order to see any motions which might be present. Since the objective is to make an estimate of the depth dependence of the zonal flow bands, it is best to have as long a time series as possible for each observation, in order to increase the signal-to-noise of the measurements. As a compromise, I divided the 792-day time series of Structure images into four parts and inverted each set of measurements separately.

The torsional oscillation is clearly visible in the measurements themselves; figure 6.12 shows measurements of the east-west time differences for the four different time periods. In each case, the large-scale variation of the time differences (equation 4.8) has been removed. The lowest curve is for measurements from May to November, 1996; the next is for the period from November, 1996 to May, 1997; the third is for measurements from May to November, 1997; and the highest curve covers the period from November, 1997 to June, 1998. The displacement between the curves was artificially added to show the time dependence of the torsional oscillation more clearly. The torsional oscillation is demonstrated in the way that the peaks and valleys in the velocity residual move toward the equator as time progresses.

To further study the torsional oscillation pattern at different depths, I inverted the measurements in figure 6.12 for each time period. Figure 6.13 shows the results. From

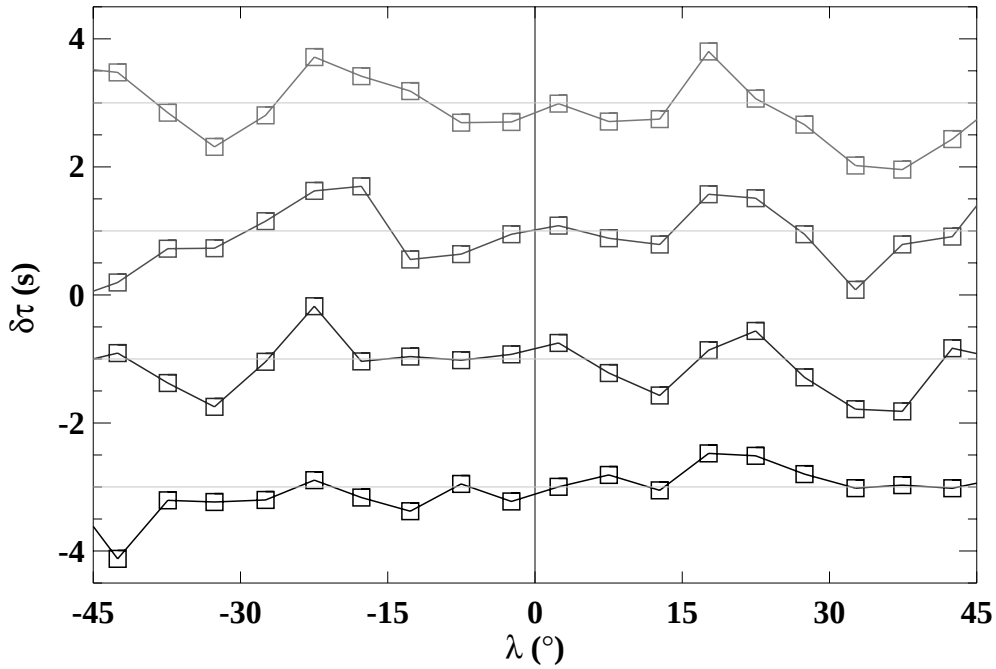

Figure 6.12: The four curves are residual time differences for the rotation measurements from four different time intervals. In each case, the time differences have had a smooth function (see equation 4.8) subtracted. The measurements shown here as a function of latitude are averaged over distances from 4 to 12 degrees. The curves have been displaced so that their mean separation is 2.5 s; time is increasing from the bottom to the top.

the velocity at each depth, I have subtracted a polynomial in even powers of $\sin\lambda$ (see equation 1.1). The upper figure shows the residuals in the surface layers, where the torsional oscillation is clearly visible. The averaging kernels for this location are reasonably well localized above $r = 0.95\,\mathrm{R}_\odot$ (see figure 6.14). The lower figure shows the residuals for the deeper layers; the averaging kernels are well localized below $r = 0.95\,\mathrm{R}_\odot$. Here there is no clear indication of the banded pattern characteristic of the torsional oscillation. This is in contrast with some recent results (Howe et al., 2000; Toomre et al., 2000) using frequency splittings, which found that the pattern is visible down to at least $r = 0.92\,\mathrm{R}_\odot$.

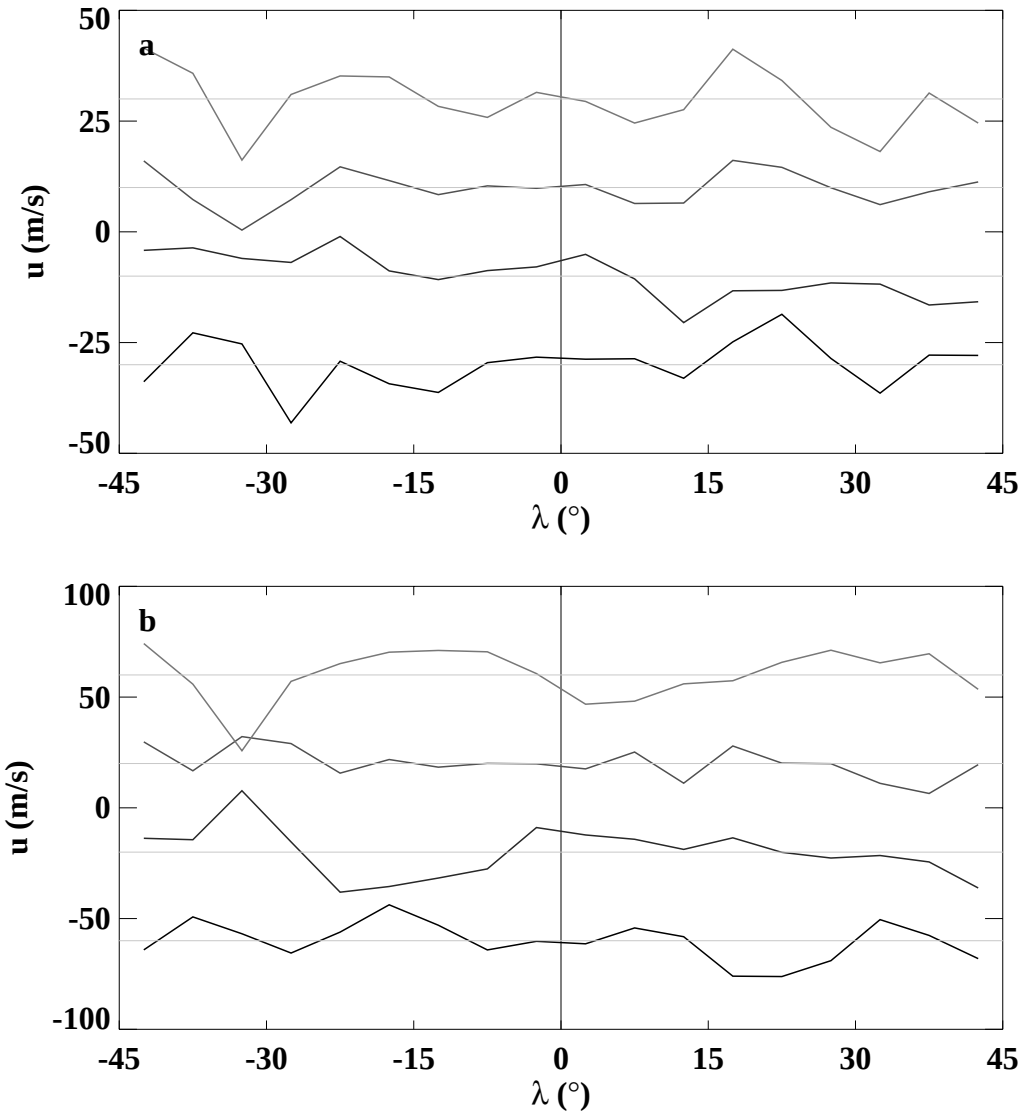

Figure 6.13: These plots show the evidence for the torsional oscillation at two different depths. The four curves in each case are for the four different time intervals, each six months long. The residuals have been displaced from zero to separate the curves. The upper plot shows the signal at the solar surface; in this region, the averaging kernels are well localized above $r = 0.95\,\mathrm{R}_\odot$. The lower plot shows the torsional oscillation for the deepest layers of the inversion, where the averaging kernels are well localized below $r = 0.95\,\mathrm{R}_\odot$ (see figure 6.14).

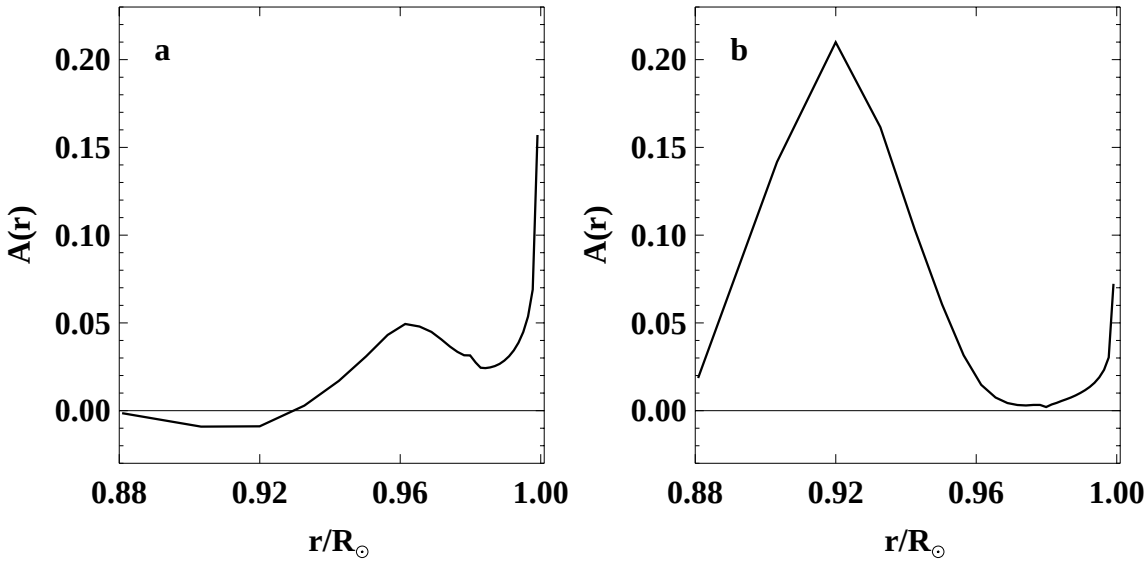

Figure 6.14: The radial cross section of the mean averaging kernels for figure 6.13(a) and (b).

Of course, there is an important difference between the two methods; the frequency splitting measurements are sensitive only to the symmetric component of the pattern, whereas these time-distance method can be used to measure the antisymmetric part as well. Figure 6.15 shows the residuals for the deeper layer again, this time decomposed into symmetric and antisymmetric components. The evidence for the torsional oscillation pattern is still not very compelling, but it is interesting to note that the lowest two curves in the upper plot and the middle two curves in the lower plot are very similar pairs. Since these four measurements should be competely independent, this may indicate some interesting time-varying patterns.

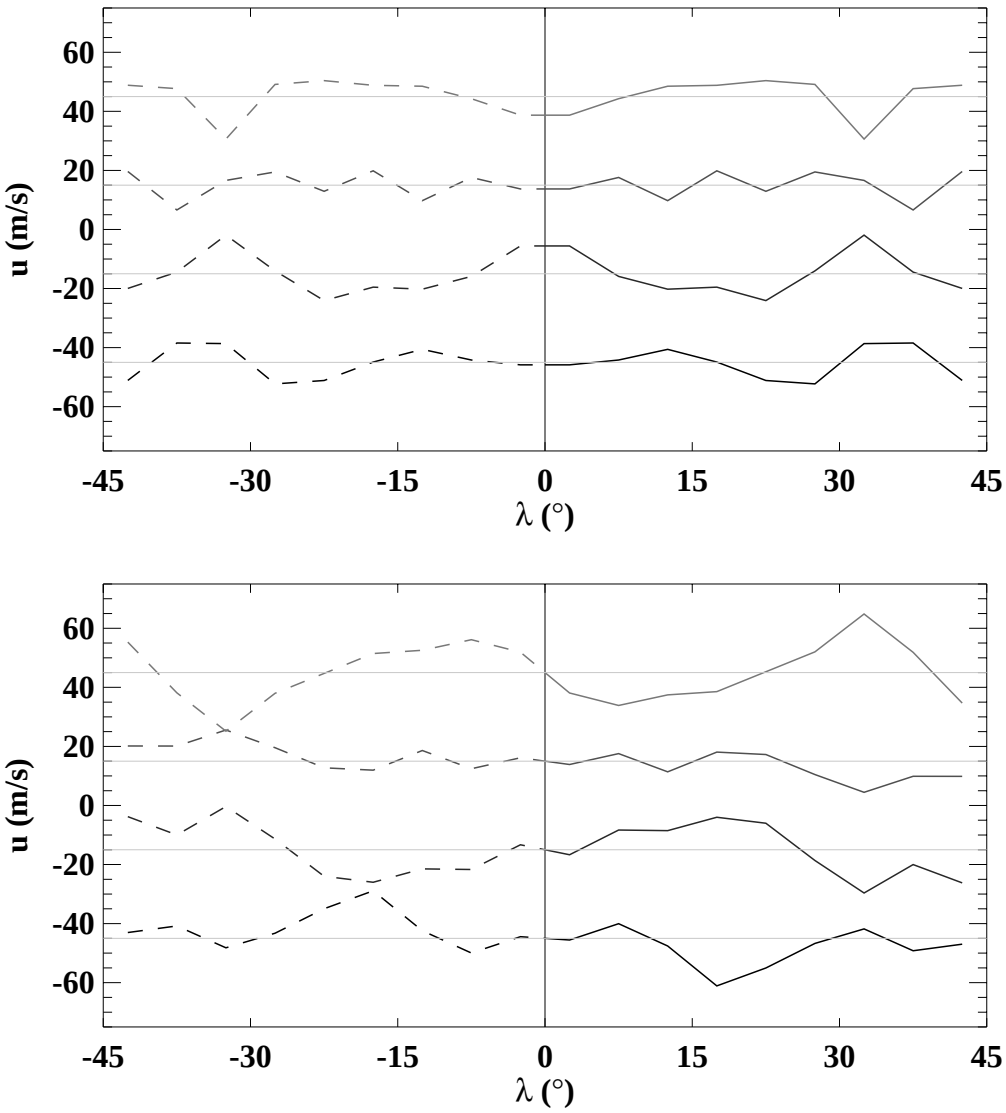

Figure 6.15: The residuals from figure 6.13 are decomposed into their symmetric (upper plot) and antisymmetric (lower plot) components.

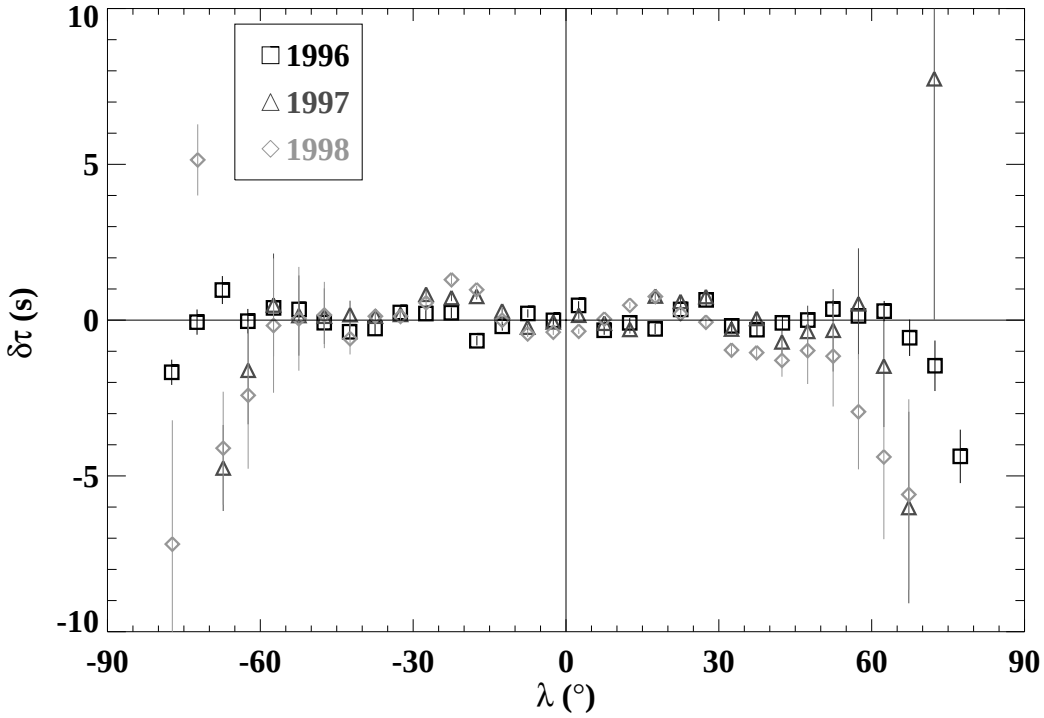

Figure 6.16: East-west time differences for the three Dynamics periods are plotted as a function of latitude. From each curve, a function of the form of equation 4.8 has been subtracted; the parameters were determined from a least-squares fit to the 1996 measurements. The distance range for these measurements is ($1^\circ \leq 6^\circ$); recall that for this range, a time difference of 1 s implies a depth-averaged velocity of 10 m/s (see figure 4.12).

6.1.5 Time variation of high-latitude rotation

Figure 6.16 shows the east-west time difference measurements for the three Dynamics periods. These measurements have had a smooth function subtracted, to emphasize the small differences between them (of course, the same function has been subtracted from all three sets of measurements). There are small variations in the flow measured at low latitude; these variations are signatures of the torsional oscillation. At high latitude, the measurements suggest that the polar rotation was decreasing during the rising phase of the solar cycle. This is in agreement with previous observations that the differential rotation is more pronounced during solar maximum.

Unfortunately, the measurements made at these latitudes have rather poor signal-to-noise, and it is not possible to resolve any depth dependence in the inversions. Future observations made from out of the ecliptic plane might be able to improve on this result.

6.2 Meridional Circulation[6]

6.2.1 Meridional circulation deep in the convection zone

Using the same time series of Structure images as described in section 6.1, I computed cross correlations for north-south pairs up to distances of 45°. The inversion procedure was also the same; the L-curve for the inversion is shown in figure 6.17. This set of inversions was performed with $H = H_{u/r}$ (see equation 5.12) in equation 5.14.

The results of the inversion are shown in figures 6.18 and 6.19. Since a travel distance of 45° corresponds to a turning point of $0.71\,R_\odot$, the model in this case extends to the base of the convection zone. The results of the inversion clearly show a poleward flow near the solar surface, with a weak dependence on radius. This is consistent with previous results from Giles *et al.* (1998) and Braun and Fan (1998). However, none of these previous results extended below about $0.88\,R_\odot$. The inversion results in figure 6.19 indicate that the poleward flow extends throughout the entire convection zone.

As with the rotation inversion results, however, it is necessary to make some comments on the limitations of the inversion results. For example, the regularization in this case will try to minimize the gradient of u/r; in areas where the sensitivity is low, or the measurement errors are large, the model will tend to show a linear variation with r. It is important also to consider the averaging kernels; some selected averaging kernels are shown in figures 6.20 and 6.21. Comparing with figures 6.4

[6]Some of the results presented in this section have been published in *Nature* (Giles et al., 1997), in the conference proceedings of IAU Symposium 185 (Giles and Duvall, 1998), and in the conference proceedings of the SOHO6/GONG98 Workshop (Giles et al., 1998). Preliminary results on the meridional circulation deep in the convection zone have been presented at the SOHO9 Workshop and are in preparation for submission to a peer reviewed journal.

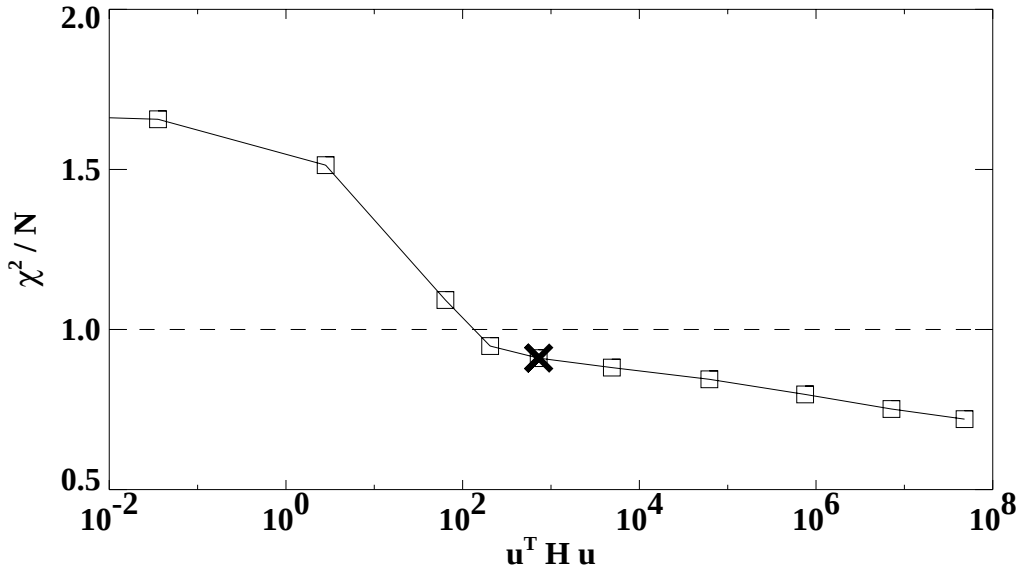

Figure 6.17: The regularization trade-off curve for an inversion of the meridional circulation.

and 6.5, it is immediately striking that the kernels for the meridional circulation are not very well localized in latitude. This is especially true at large depths, where the sensitivity for each measurement is spread over a wide range of latitudes. As a result, it would be inaccurate to state that the meridional circulation must be poleward even at the bottom of the convection zone. The next section shows another possibility which is still entirely consistent with the measurements.

6.2.2 Problem of the return flow

One important constraint on the meridional circulation profile is that mass must be conserved. That is, the flow must satisfy the continuity equation, 2.40. The results shown in figures 6.18 and 6.19 thus pose a problem; if the flow is really poleward down to the bottom of the convection zone, that would imply that the return flow is in the radiative zone.

However, an examination of the averaging kernels in figures 6.20 and 6.21 shows

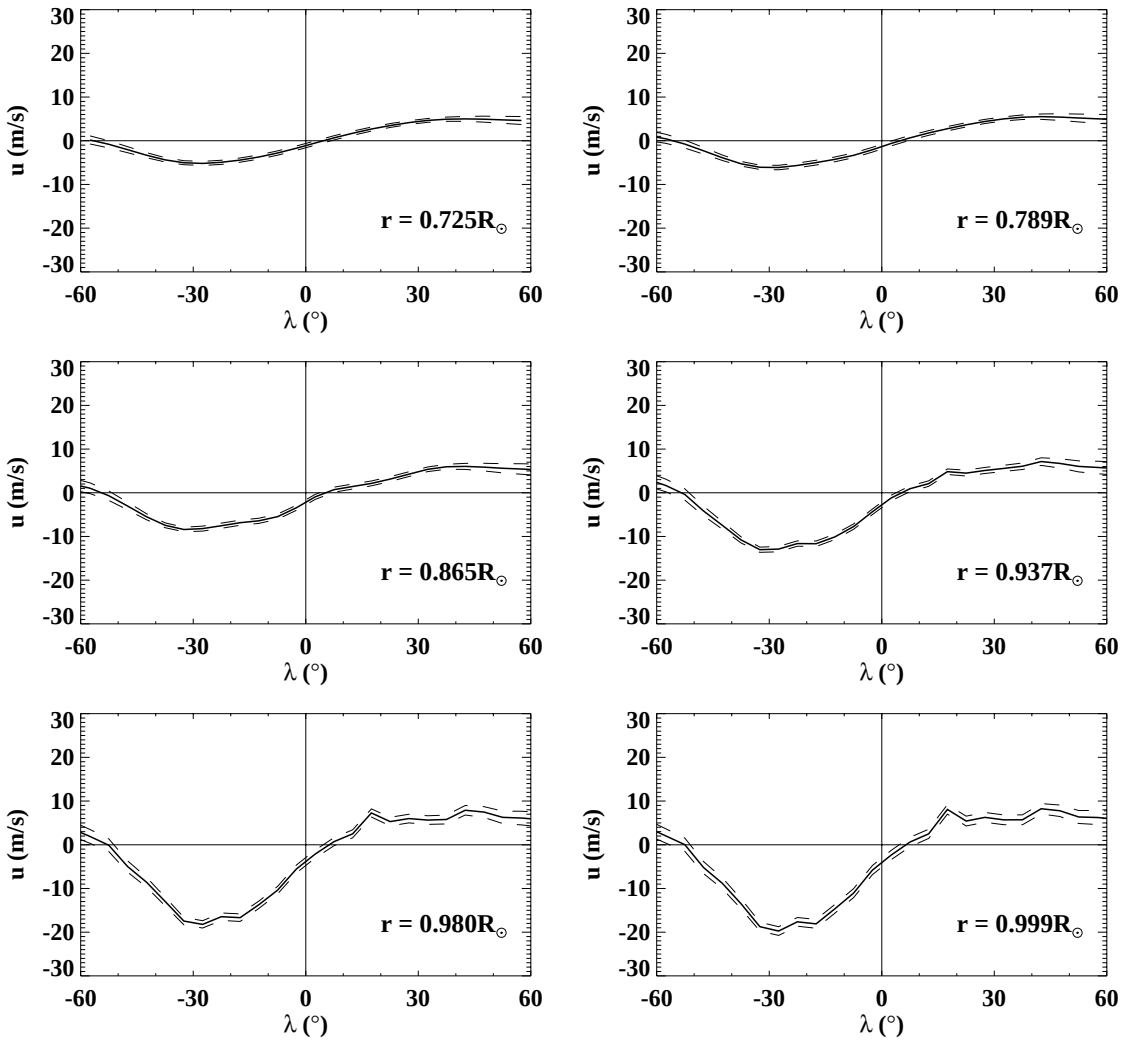

Figure 6.18: The meridional circulation inversion results, as a function of latitude λ, for six different depths. Positive velocities are northward.

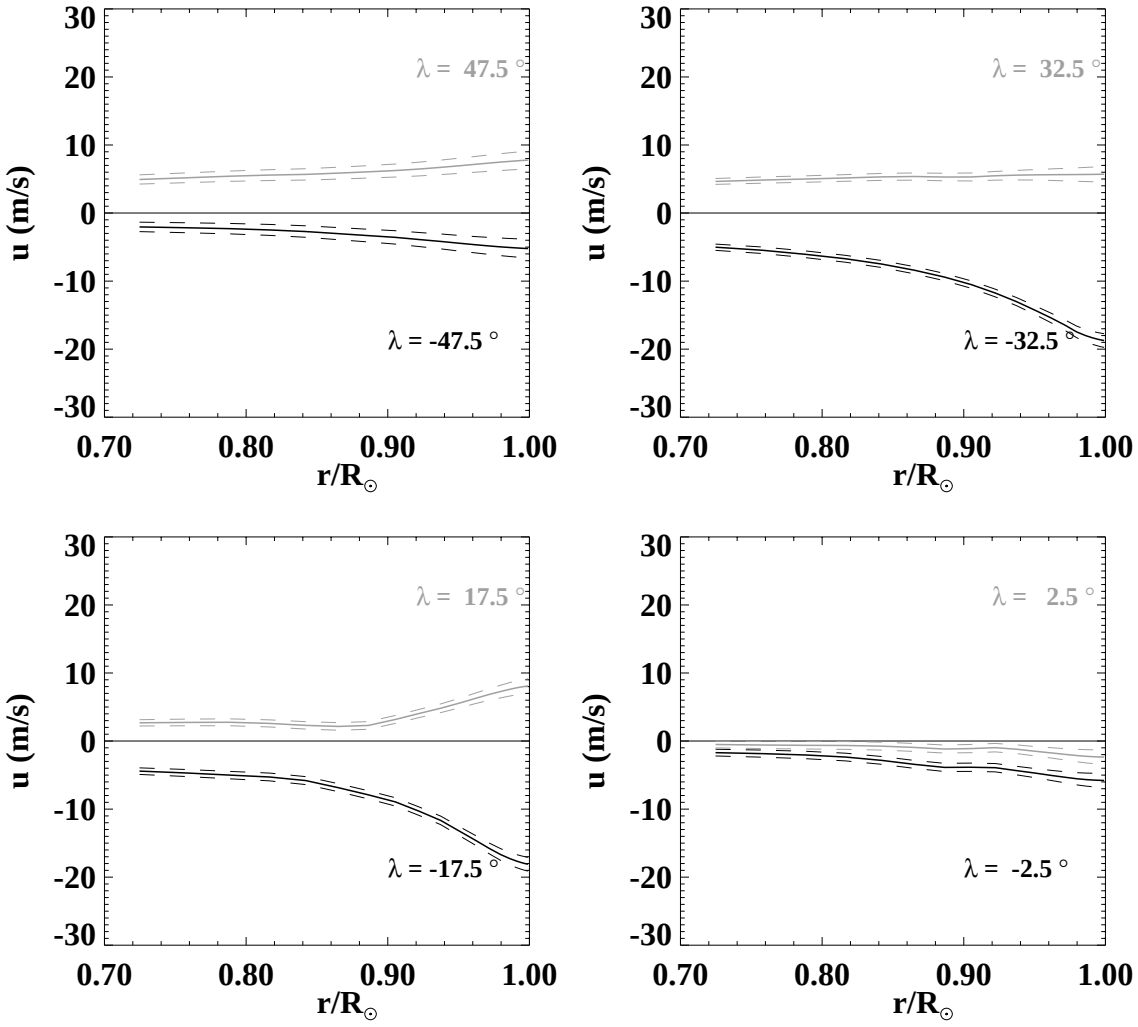

Figure 6.19: The meridional circulation inversion results, as a function of depth, for eight different latitudes. The dark curves, which are generally negative (southward) are for latitudes in the southern hemisphere; the lighter curves are for the corresponding latitudes in the northern hemisphere.

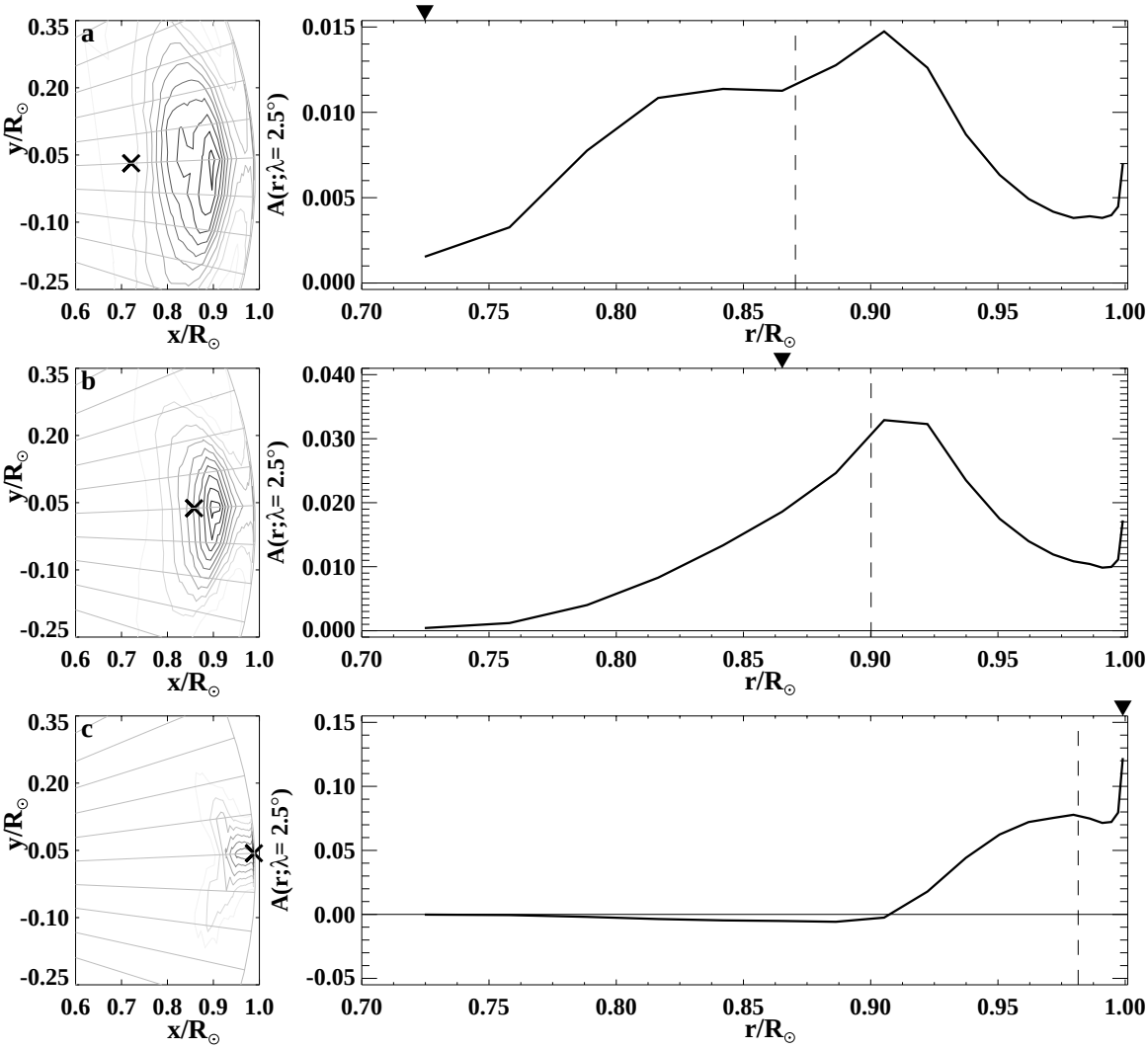

Figure 6.20: Some of the averaging kernels for the inversion results shown in figures 6.18 and 6.19. The plots in the left-hand column are contour plots of three selected averaging kernels. The contour spacing is 5% of the maximum amplitude of each kernel; dashed contours indicate a negative amplitude. The nominal locations of the three kernels, in each case marked with $\times$, are: (a) $r = 0.72\,\mathrm{R}_\odot, \lambda = 2.5°$; (b) $r = 0.87\,\mathrm{R}_\odot, \lambda = 2.5°$; and (c) $r = \mathrm{R}_\odot, \lambda = 2.5°$. In the right-hand column, a cross section of each kernel is plotted, as a function of radius, at the central latitude. The arrow above each plot marks the nominal radius of the kernel; the dashed line marks the location of the centroid.

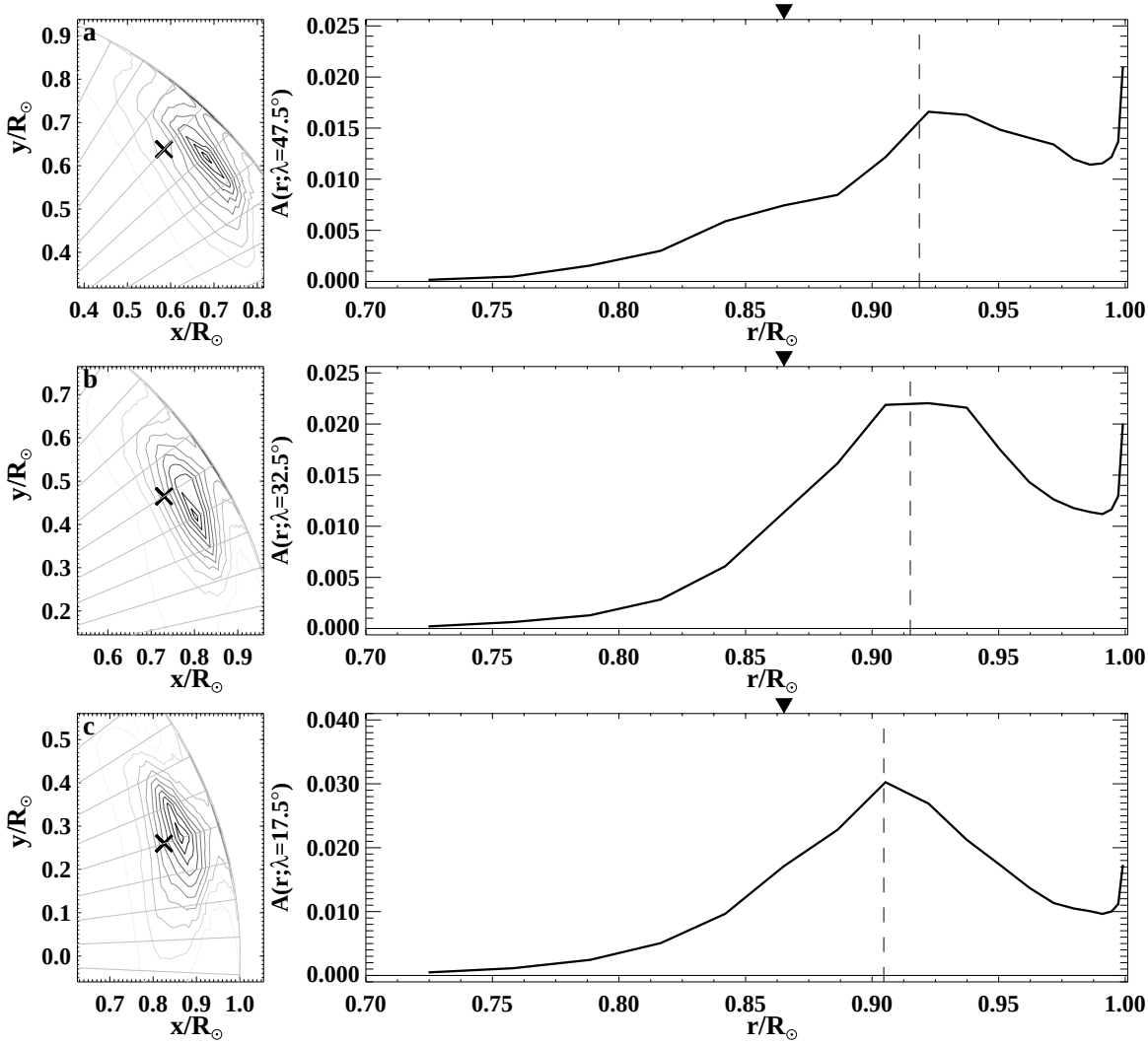

Figure 6.21: Some of the averaging kernels for the inversion results shown in figures 6.18 and 6.19. The symbols and contours are the same as for figure 6.20. In this case, the kernels all have the same nominal radius $r = 0.87\,\mathrm{R}_\odot$, but different latitudes: (a) $\lambda = 47.5°$; (b) $\lambda = 32.5°$; and (c) $\lambda = 17.5°$. Note for comparison that the nominal radius is also the same as in figure 6.20(b).

that the inversion results near the bottom of the convection zone actually contain information which spans a very wide range in radius; in fact, the averaging kernel in figure 6.20(a) has a very small amplitude at its nominal location of $r = 0.72\,\mathrm{R}_\odot$.

As explained in section 5.3, it is possible to constrain the inversion so that the solution must obey conservation of mass. When this constraint is added to the problem, new solutions can be generated which conserve mass and still satisfy the time-distance measurements. The "best" solution, in terms of the regularization condition, which satisfies the mass constraint is shown in figures 6.22 and 6.23. The turning point is at roughly $r = 0.80\mathrm{R}_\odot$; the amplitude of the equatorward flow at the base of the convection zone is about 3 m/s.

It is somewhat disheartening to admit that the circulation shown in figures 6.18 and 6.19 (which I will refer to as model A) and the one shown in figures 6.22 and 6.23 (model B) fit the measurements equally well. This is essentially due to the low sensitivity at the base of the convection zone, and the large errors on the measurements at large distances. For a ray with $\Delta = 45°$, the travel time difference in the two models differs by $|\delta\tau_A - \delta\tau_B| \simeq 0.1\,\mathrm{s}$. Since this is small compared to the measurement errors, the data cannot select one model in favour of the other. In the case of model B, the data for shorter distances is used to constrain the velocity in the near-surface layers, and the requirement that mass be conserved then dictates the circulation in the deepest layers.

Nevertheless, we might call model B the "best physical solution" which is consistent with the measurements. In addition, the combination of the 3 m/s equatorward flow and the $0.80\mathrm{R}_\odot$ turnover point are jointly constrained. For example, an increase in the flow amplitude would have to be matched by a lowering of the turnover, since the flow velocity in the upper layers is well-constrained by the data. It should also be noted that the models obtained with different regularization matrices H (equation 5.14) give qualitatively similar solutions.

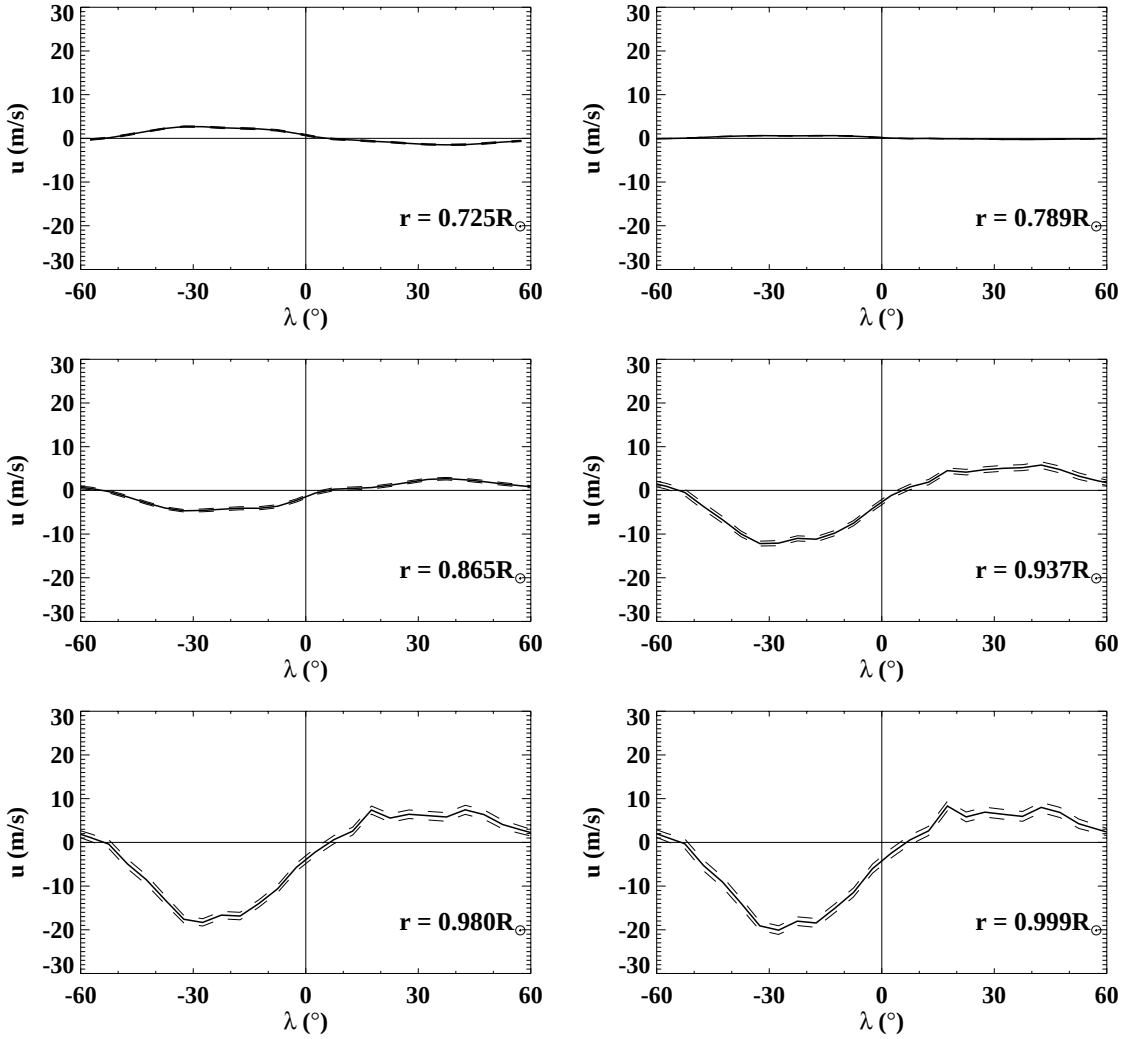

Figure 6.22: The meridional circulation inversion results, as a function of latitude λ, for six different depths. In this case, the model was constrained such that the total amount of mass moving northward is balanced by an equal amount moving southward, assuming that the velocity is zero below $0.71\,R_\odot$. Positive velocities are northward.

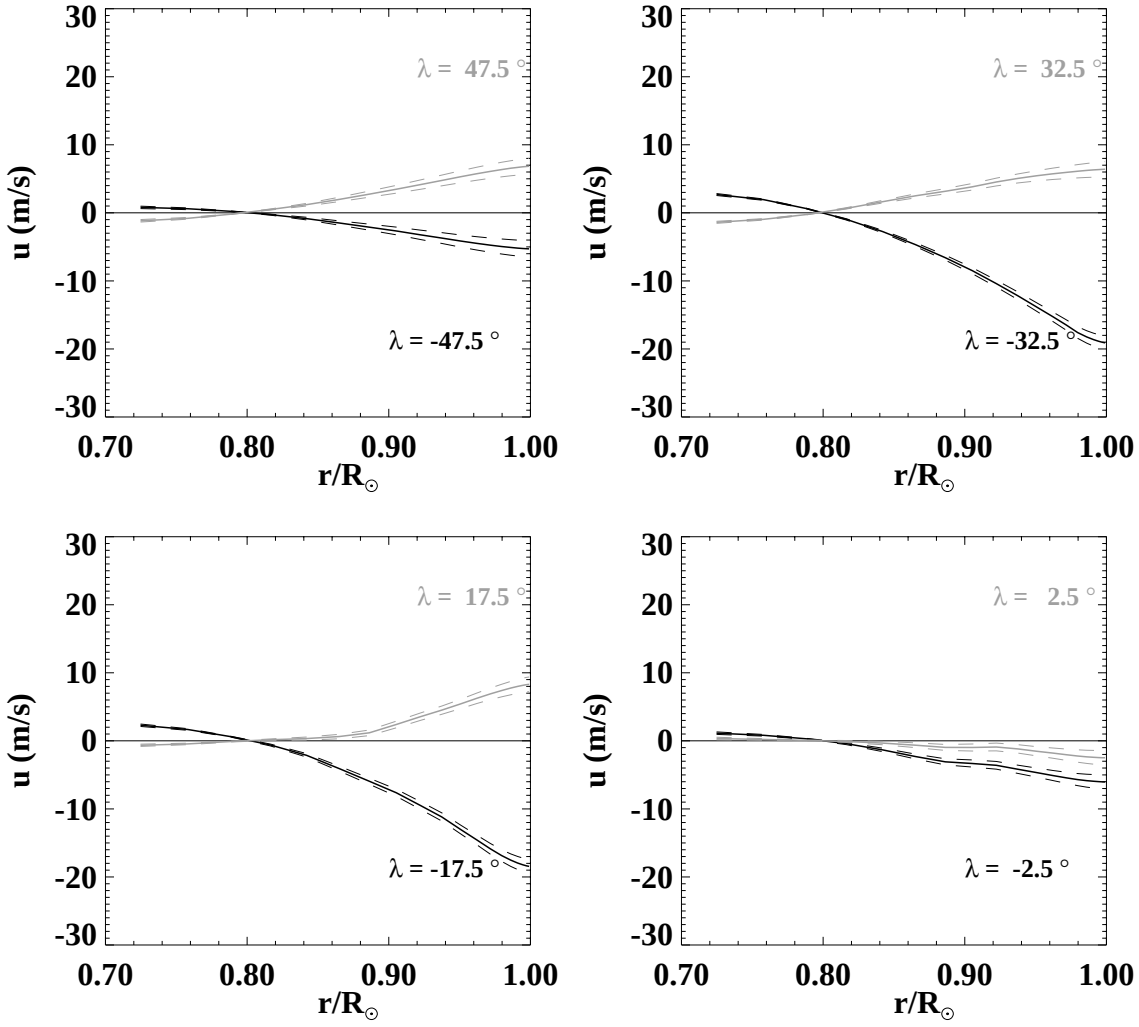

Figure 6.23: The meridional circulation inversion results for the mass-constrained case (see also figure 6.22), as a function of depth, for eight different latitudes. The dark curves, which are generally negative (southward) are for latitudes in the southern hemisphere; the lighter curves are for the corresponding latitudes in the northern hemisphere.

6.2.3 Behaviour of the equator-crossing flow

In section 4.7.1 it was pointed out that the equator-crossing (southward) meridional circulation observed with MDI may be due to an error in the orientation of the MDI image. Since the equatorial angular velocity in the convection zone is roughly independent of radius, this would result in an equator-crossing flow which was proportional to r. Figure 6.18 shows that the observed velocity is consistent with this hypothesis; however, section 6.2.2 demonstrates that quite different profiles are also consistent with the data. For the moment, it is only fair to say that the issue of the equator-crossing flow is still unresolved.

6.2.4 Time variation of meridional circulation

Since the two year observing run allows for time-resolved observations of the meridional circulation, it is interesting to examine the variation of the flow with the solar cycle. Previous observations (Komm et al., 1993b; Hathaway, 1996; Meunier, 1999) have indicated that the poleward flow observed at the surface has a smaller amplitude at solar maximum than at solar minimum.

The measurements made during the three Dynamics periods certainly show an interesting change between 1997 and 1998. Figure 6.24 shows these three sets of measurements, averaged over distance and plotted as a function of latitude. The magnetic activity was low in 1996 and 1997, but increased substantially in 1998. The amplitudes and shapes of the time difference curves are quite different; and, perhaps most interesting of all, there are hints that there is an equatorward flow in 1998 which originates near the pole and converges with the poleward flow at about 60°. The appearance of this type of two-cell pattern may be an important part of the solar cycle.

The differences in the measurements shown in figure 6.24 also appear in the inversions for meridional velocity. Figure 6.25 shows the surface velocity for these three time periods. The velocity in the inversions does not vary with depth down to $r = 0.96\,\mathrm{R}_\odot$. It would be interesting to look beyond this depth; unfortunately, considerations related to image geometry make the Structure images rather useless at

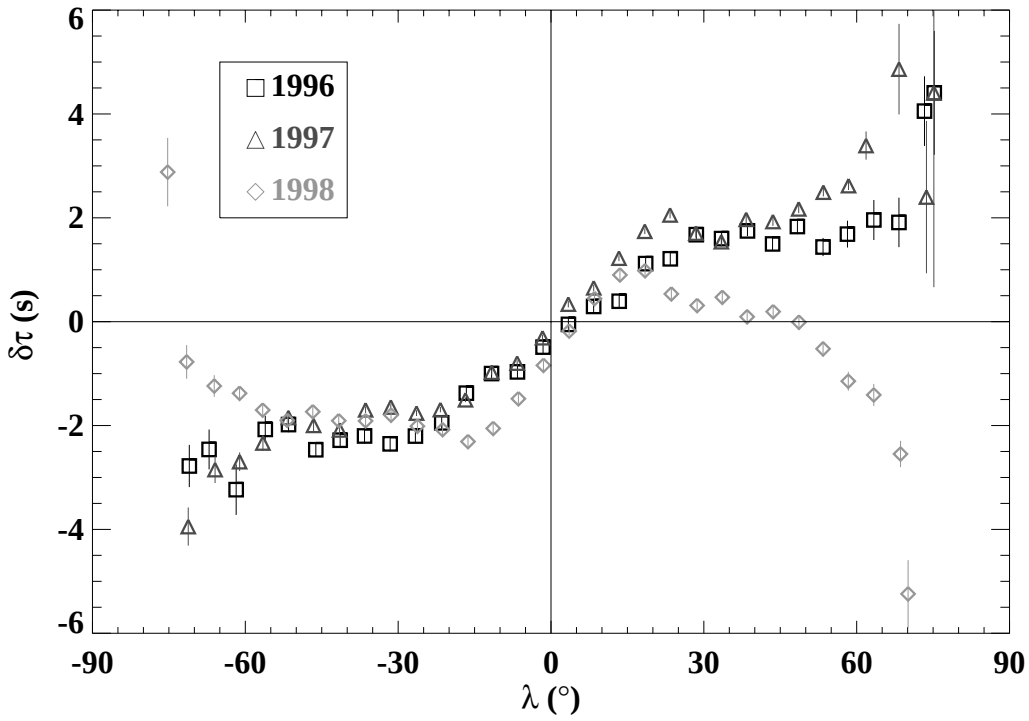

Figure 6.24: The south-north time differences as a function of latitude (see also figure 4.11) are plotted for three different Dynamics periods. These measurements were averaged in distance over a range ($1° \leq \Delta \leq 6°$). The sense of the time difference is south $-$ north, so that a positive time difference indicates a northward flow. For reference, a time difference $\delta\tau = 1\,\mathrm{s}$ indicates a flow of about $10\,\mathrm{m/s}$; a distance of $\Delta = 6°$ corresponds to an inner turning point at $r = 0.963\,\mathrm{R}_\odot$.

high latitude. The depth dependence of this possible two-cell pattern will probably remain unresolved until observations can be made from a position out of the ecliptic plane.

A final comment should be made about the equator-crossing flow. Figure 6.25 shows a time variation in this flow, with a larger amplitude in 1998 than in 1997 or 1996. However, most of this variation can be accounted for by an error in the Carrington elements. This is discussed further in appendix A.

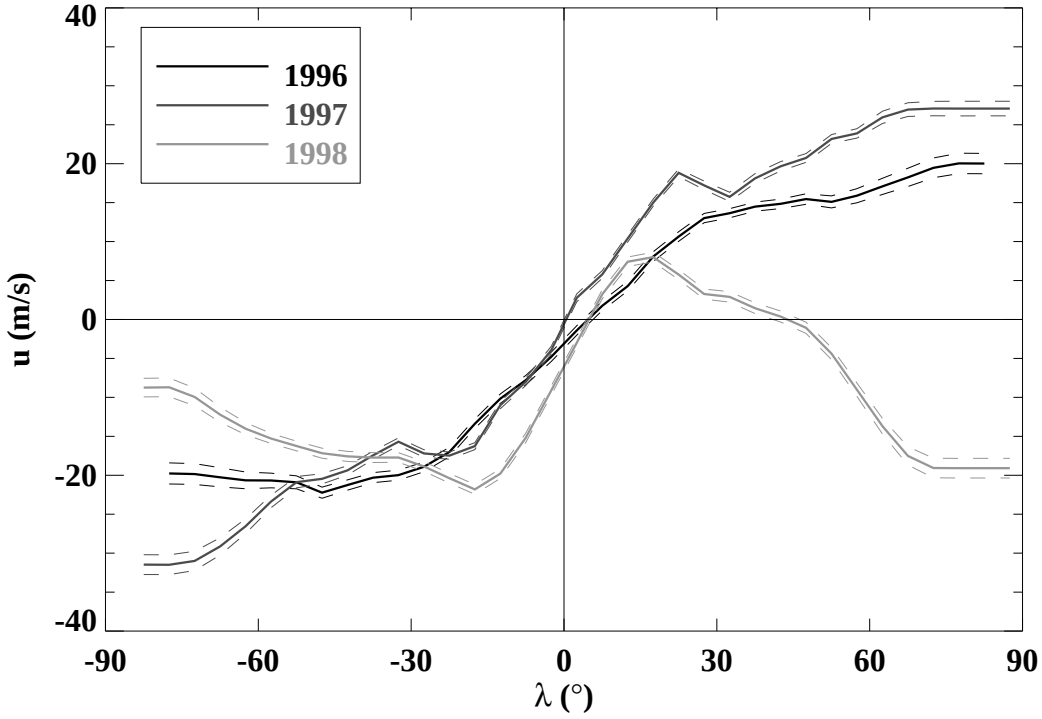

Figure 6.25: The inversion results for the three Dynamics periods. The velocity u is plotted as a function of latitude, for radius $r = \mathrm{R}_\odot$. The inversion resuts do not show any significant depth dependence for the region covered by these rays (down to $r = 0.96\,\mathrm{R}_\odot$).